Energy Advances

ROYAL SOCIETY OF CHEMISTRY

PAPER

View Article Online
View Journal

Cite this: DOI: 10.1039/d6ya00089d

Cyclic ether-based electrolyte solutions for potassium metal batteries

Roy Heyns, [a] Robert Markowski, [b] Andrii Kachmar, [b] Johannes Ingenmey, [c] Wouter Monnens, [d] Alexandru Vlad, [be] Barbara Kirchner, [c] Jan Fransaer [d] and Koen Binnemans *[a]

Received 28th March 2026,
Accepted 14th May 2026

DOI: 10.1039/d6ya00089d

rsc.li/energy-advances

Potassium metal batteries (KMBs) are promising candidates for large-scale energy storage due to the high abundance of potassium and its very low reduction potential. However, poor reversibility during plating and stripping due to the high reactivity of the potassium metal anode and the formation of an unstable solid electrolyte interphase (SEI) hinders their practical implementation. This work conducts a comparative analysis of two electrolyte solutions based on weakly coordinating solvents, consisting of potassium bis(fluorosulfonyl)imide (KFSI) in tetrahydrofuran (THF) and 2-methyltetrahydrofuran (MeTHF). The physical and electrochemical properties of these electrolyte solutions, as well as the plating and stripping behavior of potassium metal on aluminum current collectors, were investigated. Furthermore, this study attempts to demonstrate how solvent structure modulates solvation behavior, which governs SEI formation and thereby determines electrochemical performance. Both electrolyte solutions enabled reversible potassium metal plating/stripping, achieving a coulombic efficiency (CE) of about 99% for 500 cycles at 0.5 mA cm^{-2} and 1 mAh cm^{-2}. Spectroscopic analysis unveiled the formation of contact ion pairs (CIPs) and aggregates (AGGs), resulting in the formation of an anion-derived SEI. Cycling in full cells with an organic cathode material gave the proof of concept for the application of these electrolyte solutions in potassium metal batteries.

1. Introduction

Lithium-ion batteries (LIBs) are widely used as a desirable energy storage system in portable devices and electric vehicles.[1] Although LIBs currently dominate the electrochemical energy storage worldwide, the long-term availability of lithium is a challenge due to the low abundance of lithium in the Earth's crust and the uneven geographical distribution of available lithium reserves.[2,3] In the last decade, the focus on battery research has shifted to low-cost and material-abundant alternatives like sodium-ion batteries (NIBs).[4] More recently, potassium-ion batteries (KIBs) have gained much more attention as a post-LIB alternative because of the higher abundance of potassium resources and the unique properties of the K^+ ion as a charge carrier.[5,6] One of the important advantages of KIBs is the reduction potential of the K^+/K redox couple in organic electrolyte solutions, which is even more negative than the reduction potential of the Li^+/Li redox couple.[7–9] Furthermore, the lower Lewis acidity of the K^+ cations compared to that of Li^+ and Na^+, results in the formation of much smaller solvated ions. The weaker interaction between the K^+ ions and the solvent molecules leads to a higher ionic conductivity of the electrolyte solutions compared to solvated Li^+ ions or Na^+ ions.[10,11] K^+ ions, like Li^+ ions, can reversibly (de)intercalate in between the graphite layers of the anode, whereas the intercalation of Na^+ ions is thermodynamically unfavorable.[12,13] A new architecture of battery technology is anode-free metal batteries, which rely solely on the current collector at the anode. During charging, K^+ ions from the cathode are deposited on the current collector, and the deposited potassium metal serves as the anode, resulting in a higher energy density of potassium metal batteries (KMBs) compared to that of KIBs.[14] However, achieving high reversibility during the plating/stripping of potassium metal on a bare current collector is challenging due to the formation of an unstable solid electrolyte interphase (SEI) and uncontrolled dendrite growth.[15–18] A common baseline electrolyte solution used for potassium battery research is 0.8 M KPF_6-EC/DEC, yet it does not support stable potassium metal plating and stripping, typically reaching only 10–20 cycles before cell

[a] KU Leuven, Department of Chemistry, Celestijnenlaan 200F, P.O. box 2404, B-3001 Leuven, Belgium. E-mail: Koen.Binnemans@kuleuven.be
[b] UC Louvain, Institute of Condensed Matter and Nanosciences, Place L. Pasteur 1, Lavoisier Building, B-1348 Louvain-la-Neuve, Belgium
[c] University of Bonn, Mulliken Center for Theoretical Chemistry, Bonn D-53115, Germany
[d] KU Leuven, Department of Materials Engineering, Kasteelpark Arenberg 44, P. O. box 2450, B-3001 Leuven, Belgium
[e] WEL Research Institute, avenue Pasteur, 6, 1300 Wavre, Belgium

failure. Therefore, developing an electrolyte solution that forms a stable interface between the electrolyte solution and the reactive potassium metal anode is essential to ensure good battery performance. These challenges can be improved by using ether-based electrolyte solutions. Compared to carbonate solvents, ether solvents exhibit an exceptional reduction stability, resulting in the formation of a thin and dense SEI layer at the anode interface to ensure long-term cyclability. Nevertheless, ether-based electrolyte solutions have low thermal stability and their oxidation stability is inferior to that of carbonate solvents, leading to oxidative decomposition above +4 V.[19] These inherent shortcomings can be improved by manipulating the electrolyte solution. Highly concentrated electrolytes (HCEs) are one of the possible candidates that can improve the shortcomings of conventional electrolyte solutions.[20] In HCEs, the solvent molecules and the anions coordinate to the cation, forming a unique solvation structure consisting of contact ion pairs (CIPs: solvation shell containing one anionic group) and aggregates (AGGs: solvation shell containing two or more anionic groups). The unique solvation structure in HCEs contributes to a new electrolyte design with advanced properties for next-generation batteries. The CIPs and AGGs will preferentially decompose over the free solvent molecules, leading to an anion-derived robust inorganic-rich SEI that minimizes the dendritic growth of potassium metal.[21–23] HCEs have different chemical and physical properties compared to their dilute counterparts, such as increased oxidation/reduction stability, non-corrosiveness towards aluminum current collectors, decreased flammability/volatility and high charge carrier density.[24] A popular class of solvents used for the preparation of HCEs are oligoethylene glycol dimethyl ethers, also called glymes, due to their excellent solvating properties and their exceptional cathodic and chemical stability. These linear ether solvents, such as 1,2-dimethoxyethane (DME, monoglyme, G1), diethylene glycol dimethyl ether (DEGDME, diglyme, G2) and triethylene glycol dimethyl ether (triglyme, G3), have been extensively studied. Xiao *et al.* first demonstrated the use of a HCE consisting of KFSI in 1,2-dimethoxyethane (DME, G1, monoglyme) at a solvent-to-salt molar ratio of 2 : 1. In an asymmetrical K‖Cu coin cell, this HCE enabled stable, dendrite-free potassium metal deposition on the copper current collector with a CE of 99%.[25] Increasing the glyme length enhanced the oxidation stability of the HCEs, leading to improved cycling stability of full cells.[26] Later, a HCE consisting of 4 M KFSI in DEGDME was reported by Xu *et al.*, which enabled stable cycling of potassium metal anodes with a high CE over 98% in K‖Cu coin cells.[27]

Although linear ethers are often used as the preferred solvent for electrolyte solutions in batteries, cyclic ethers such as THF offer several advantages. The bulky ring structure and monodentate coordination mechanism of cyclic ethers make them act as weakly coordinating solvents. The use of cyclic ethers in electrolyte solutions promotes anion-rich solvation structures, resulting in the formation of a stable anion-derived SEI during cycling, and offers therefore an alternative for HCEs. Furthermore, the higher costs and viscosity limitations of HCEs are avoided, while the unique solvation structure is retained.[28]

In order to develop more sustainable electrolyte solutions, 'greener' chemicals must be used instead of conventional solvents like glymes or THF. A greener and safer alternative to THF is MeTHF, which is an easily available, inexpensive, neoteric, bio-based solvent. MeTHF can be extracted from precursors such as furfural or levulinic acid derived from renewable sources (*e.g.*, corn cobs or bagasse), satisfying Principle 7 of the 12 Principles of Green Chemistry.[29,30] Unlike lithium, potassium does not form alloys with aluminum at low potentials, which eliminates the use of copper current collectors at the anode.[31,32] The use of aluminum significantly reduces the overall mass of the battery, as aluminum has a much lower theoretical density ($\sim$2.7 g cm^{-3}) than copper ($\sim$8.9 g cm^{-3}), thereby improving the energy density of the battery. Furthermore, aluminum is cheaper and more abundant than copper, which make it also economically attractive.

This work explores the physical and electrochemical properties of two cyclic ether-based electrolyte solutions consisting of KFSI in THF and MeTHF at solvent-to-salt ratios of 3 : 1 and 4 : 1, respectively. These electrolytes are homogeneous solutions, yet close to the solubility limit. The greener MeTHF solvent is compared with its more harmful analogue THF for enhancing the potential of potassium metal batteries using aluminum as a current collector at the anode.

2. Experimental section

2.1. Materials and chemicals

Potassium bis(fluorosulfonyl)imide (KFSI, 99.9%, extra-dry) was purchased from Solvionic (Toulouse, France) and was used as received. Tetrahydrofuran (THF, battery grade, min. 99.9%) and 2-methyltetrahydrofuran (BioRenewable, anhydrous, $\geq$99%, inhibitor-free) were purchased from DoDoChem (Jiangsu, China) and Sigma-Aldrich (Diegem, Belgium), respectively. All solvents were dried prior to use over freshly activated molecular sieves 3 Å, 1 to 2 mm beads), which were purchased from Thermo Scientific (Kandel, Germany). High purity electrode potassium metal chips (99.7%, 0.45 mm in thickness, 14 mm in diameter) were purchased from Xiamen AOT Electronics Technology Co., Ltd (Hong Kong, China) and were used as received. Coin cell spares (stainless steel, SS-316) were purchased from TOB New Energy Technology Co., Ltd (Xiamen, China). Aluminum foil (Al, 12 mm in thickness) was purchased from Shenzhen Tianchenghe Technology Co., Ltd (China). Celgard 2400 monolayer microporous membrane polypropylene (PP) and glass microfiber (GF/D) separators were purchased from Celgard Corporation and Whatman, respectively.

2.2. Preparation of electrolyte solutions

The electrolyte solutions were prepared by adding a stoichiometric amount of solvent (THF or MeTHF) to KFSI. Solvent-to-salt mole ratios were used for the concentration notations of

the electrolyte solutions. All electrolyte solutions were prepared in a glovebox filled with argon (O_2 < 1 ppm; H_2O < 1 ppm).

2.3. Characterization of electrolyte solutions

The viscosity and density of the electrolyte solutions were measured on a Anton Paar Lovis 2000 ME microviscometer and a DMA 4500 M density meter, respectively. To avoid contact with air, the samples were transferred from their sealed argon-filled containers to a 1 mL syringe and subsequently injected into the capillaries (∅ = 1.8 mm or ∅ = 1.59 mm) and the density chamber of the device. The temperature during both the viscosity and density measurements was set to 25 °C and controlled using the internal thermostat of the device.

The ionic conductivity of the electrolyte solutions was measured using a Mettler-Toledo SevenExcellence Multiparameter conductivity meter equipped with an InLab 751-4 mm glass probe with two platinum poles. The instrument was calibrated using aqueous standards with known conductivity (1413 mS cm^{-1} or 12.88 mS cm^{-1}). A conductivity standard of 5000 mS cm^{-1} at 25 °C (±1%) was used for verification. The probe was submerged in the electrolyte solutions at ambient temperature (~25 °C) and the setup was allowed to stabilize. Contact of the samples with ambient air was unavoidable during the measurement. For each sample, the exposure time to the air was less than 20 seconds.

FT-Raman spectra were recorded between 3500 cm^{-1} and 50 cm^{-1} on a Bruker Vertex 70 spectrometer with a RamII module and a liquid-nitrogen-cooled germanium diode detector. Each measurement consisted of 200 scans at a resolution of 2 cm^{-1} with a 1064.38 nm laser (Nd:YAG) at a power of 500 mW. Samples were measured inside 1.5 mL glass vials that were filled inside the glovebox and closed with airtight screwcaps. All spectra were individually, vertically scaled to equal the intensity of the largest signal.

High-field nuclear magnetic resonance (NMR) spectra were recorded on a Bruker Avance Neo 600 spectrometer with an Ascend™ 600 magnet system and a 5 mm PI HR-TBO (BB/F-H/F-D) probe with *z*-gradients. All samples were prepared inside a glovebox by filling screw-cap NMR tubes (5 mm OD) with the electrolyte solutions to retain a pure argon atmosphere. Deuterium oxide (D_2O) was used as an external reference in a capillary. Data were recorded at room temperature (298 K) using TopSpin 4.4.1 and processed and analyzed using Bruker TopSpin 4.5.0. The δ-values are expressed in parts per million (ppm). All spectra were individually, vertically scaled to equal the intensity of the largest signal.

2.4. Coin cell assembly and electrochemical measurements

Stainless steel (SS) SS316-grade CR2032-coin cell cases were used for constructing half-cells. K‖Al asymmetric cells were assembled for electrochemical measurements, using aluminum foil as the working electrode (side of the positive case) and a potassium metal chip as both the counter and the reference electrode (side of the negative case). Aluminum foil was cut into circular sheets of 16 mm in diameter and pre-treated with ethanol (analytical reagent grade, absolute., ≧99.8%). A glass microfiber GF/D with a diameter of 19 mm was used as the separator and 100 μL of the electrolyte solution was added to each coin cell. Subsequently, a 316SS spacer (∅ = 15.8 mm; *t* = 1 mm) and a 316SS conical spring (∅ = 15.4 mm; *t* = 1.2 mm) were placed on top of the potassium metal chip. Finally, a stainless-steel cap with an insulating gasket (negative case) was added. The coin cells were crimped at an applied pressure of 750 kg using an electronically controlled crimping machine. Following assembly, the cells were allowed to rest for 5 hours to establish a stable open circuit potential (OCP).

Cyclic voltammetry (CV) tests of K‖Al half-cells were performed using a BioLogic VSP-3e potentiostat. The potential was swept from the OCP to −0.4 V *vs.* K^+/K at a scan rate of 1.0 mV s^{-1}.

Galvanostatic potassium metal plating/stripping was performed in K‖Al half-cell configuration cycled in the electrolyte solution at different current densities (0.5 mA cm^{-2}; 1.0 mA cm^{-2}; 2.0 mA cm^{-2} and 4.0 mA cm^{-2}) with a cutoff capacity of 1 mAh cm^{-2} and a charging cutoff voltage of +1.0 V *vs.* K^+/K.

In addition, galvanostatic cycling tests using K_2-Co-benzene-1,2,4,5-tetra-methylsulfonamide (K_2-Co-PTtSA) as the cathode material were carried out in CR2032-type coin cells with a 13 mm diameter active carbon fabric (AC) or a 14 mm potassium metal chip as the counter/reference electrode. The positive electrode was prepared by grinding 50 wt% active cathode material with 40 wt% conductive carbon (Super P) and 10 wt% PTFE as a binder.[33] The composite powder was applied to the positive side of the coin cell case and compacted with a stainless-steel disc. The loading of the active cathode material was approximately 3 mg, with a surface density of about 2–3 mg cm^{-2}. The coin cells were cycled at 0.1C, 0.2C, 0.5C, 1C, 2C, 5C and 10C (with 1C corresponding to a current density of 100 mA g^{-1}), for 5 cycles each. After the C-rate experiment, a long-term stability test was performed at a cycling rate of 1C. All galvanostatic cycling experiments were conducted using Neware battery testing equipment and performed at room temperature. THF–KFSI 3 : 1 and MeTHF–KFSI 4 : 1 were used as electrolyte solutions.

2.5. Surface characterization

To study the morphology of the deposited potassium metal and the SEI, a Celgard 2400 membrane with a diameter of 19 mm was placed between the aluminum foil and the glass microfiber GF/D separator to avoid GF/D sticking with potassium metal, which would destroy the deposition morphology. Cycled electrodes were retrieved from the disassembled coin cells, rinsed with the solvent of which the electrolyte solution was made (THF or MeTHF), and left to dry inside a glove box.

The morphology of the potassium metal deposits was studied by scanning electron microscopy (SEM) using the FEI Nova 600 Nanolab. SEM images of the potassium metal deposits were obtained using the SE mode at an acceleration voltage of 10.00 kV using a TLD detector with magnifications of 1200× and 10 000×. Elemental analysis was done with energy-dispersive X-ray spectroscopy (EDX) using an octane elite super silicon drift detector (Ametek EDAX).

A cross-section of the deposited potassium metal was obtained using a JEOL IB-09010CP cross-section polisher. The specimen was covered with a shielding plate and an ion

accelerating voltage of 6.00 kV was applied with a processing time of 3 hours. The samples were prepared in an argon-filled glove box, packed in argon-filled glass vials and quickly transferred into the SEM vacuum chamber with minimal exposure to ambient atmosphere.

To study the SEI, X-ray photoelectron spectroscopy (XPS) was performed using a PHI Genesis Fully Automated Multi-Technique Scanning XPS/HAXPES Microprobe with a Cr Kα (5414.8 eV) X-ray source. The samples were prepared in an argon-filled glove box and transferred into the chamber *via* an argon-filled transfer container to avoid exposure to ambient atmosphere.

X-ray diffraction (XRD) patterns were collected using a Bruker D2 Phaser, equipped with a Cu-Kα source (λ = 0.154184 nm) in the 2θ range of $10^\circ < 2\theta < 60^\circ$ with a step size of 0.01°. The samples were prepared in an argon-filled glove box and covered with Kapton tape. Adhesive putty was used to fix the sample in the Bruker PMMA ring sample holder (specimen well: 40 mm diameter). A Bruker silicon low background sample holder was used to measure the XRD pattern of the Kapton tape.

2.6. Theoretical calculations

Classical molecular dynamics (MD) simulations were performed using the LAMMPS program package (version of 23 June 2022).[34] Bulk simulations of KFSI in THF and MeTHF at solvent-to-salt ratios of 3 : 1 and 4 : 1, respectively, were carried out in cubic boxes under periodic boundary conditions in all dimensions. Five replica simulations with independent initial configurations were performed for each electrolyte solution. The composition and equilibrated box dimensions of the simulated systems are reported in Table S3 in the supplementary information (SI). OPLS-AA force field parameters were employed for THF, MeTHF, and the K^+ cation.[35,36] Parameters for the FSI^- anion were taken from the Cl&P force field.[37] Non-bonded interactions between unlike atoms were computed using geometric mixing rules. The cutoff for Lennard-Jones and coulombic interactions was set to 1.2 nm. The initial configurations were created using the PACKMOL tool, by randomly distributing molecules within a cubic box with a volume 20% larger than the sum of the components' van der Waals volumes.[38] The systems were equilibrated over a total simulation time of 18 ns in the NVE, NpT, and NVT ensembles. After an initial energy minimization, the systems were simulated for 250 ps in the NVE ensemble with added velocity scaling corresponding to a temperature of 500 K, to smooth out residual energetic hotspots. Afterwards, the systems were simulated for 8 ns in the NpT ensemble. The Nosé–Hoover chain thermostat and barostat were applied to ensure an average pressure of 1.01325 bar and a temperature of 298.15 K.[39,40] The average volume of the latter 5 ns was then used as the final box volume for the subsequent equilibration run of 10 ns in the NVT ensemble. Finally, a production run of 10 ns was carried out in the NVT ensemble. The timestep was set to 0.5 fs and atomic coordinates were dumped every 1000th step to a trajectory file for further processing. Radial distribution functions and neighbor count analyses were computed using the MD post-processing tool TRAVIS.[41,42]

3. Discussion

3.1. Physicochemical properties of THF/MeTHF–KFSI electrolyte solutions

Binary mixtures of THF and MeTHF with KFSI were prepared at solvent-to-KFSI mole ratios ranging from 50 : 1 to 2 : 1. Even at high concentrations of KFSI, homogeneous liquid mixtures were obtained, indicating a high solubility in these cyclic ether solvents. The excellent solubility of KFSI can in part be explained by the electron-withdrawing properties of the $-SO_2F$ groups in the anion, resulting in efficient delocalization of the charge of the anion. For the THF-based mixtures, saturation occurred at a solvent-to-KFSI mole ratio of 2 : 1, while for the MeTHF-based mixtures, saturation already occurred at a solvent-to-KFSI mole ratio of 3 : 1. These ratios correspond to K^+ concentrations of 2.94 mol L^{-1} and 2.02 mol L^{-1}, respectively.

To assess the suitability of these THF/MeTHF–KFSI binary mixtures as potential electrolyte solutions in batteries, their physicochemical properties such as ionic conductivity (κ), dynamic viscosity (η), density (ρ), and K^+ concentration (c_{K^+}) were determined (Tables S1 and S2). Fig. S1a shows the ionic conductivity and the dynamic viscosity of the electrolyte solutions as a function of K^+ concentration for THF and MeTHF. The ionic conductivity is one of the most important properties of an electrolyte solution, since it has a significant influence on the current densities that can be achieved in cells. Essentially, the ionic conductivity of an electrolyte solution depends on the total concentration of charge carriers (ions) and the mobility of those charge carriers. In turn, ion mobility depends on the dynamic viscosity of the electrolyte solution, whereby these values change depending on the concentration of the salt and the nature of the solvate species present in the solution. Fig. S1a shows that the dynamic viscosity curves for both series of electrolyte solutions nearly coincide. Despite the similar trend in viscosity for both electrolyte solutions, there is a significant difference in the ionic conductivity curves. For the THF-based electrolyte solutions, a maximum in ionic conductivity is reached at a solvent-to-KFSI mole ratio of 6 : 1, which corresponds to a K^+ concentration of 1.72 mol L^{-1}. However, for the MeTHF-based electrolyte solutions, a maximum in ionic conductivity is reached at maximum solubility, as the ionic conductivity continues to increase with increasing K^+ concentration. Upon increasing the K^+ concentration in THF, the ionic conductivity increases as the increase in viscosity is relatively small. Beyond the maximum, the ionic conductivity decreases due to the strong increase in the dynamic viscosity, resulting in less mobile solvate structures. In addition, it is evident that the ionic conductivity of the THF-based electrolyte solutions is manyfold higher than that of the MeTHF-based electrolyte solutions. This substantial difference can be explained by differences in the solvation structures that are present in the solution, *i.e.*, a higher degree of contact ion pair (CIP) and aggregate (AGG)

formation in the MeTHF-based electrolyte solutions. Neutral species such as CIPs are not attracted to the electrodes, unlike charged species such as solvent-separated ion pairs (SSIPs). Fig. S1b shows the Walden plot for the THF/MeTHF–KFSI binary mixtures obtained from the dynamic viscosity and the ionic conductivity. The Walden plot is an instructive method to determine the degree of ion association or ionicity of electrolyte solutions.[43,44] The idealized aqueous reference KCl line represents a solution in which ions are fully dissociated and ion transport follows viscous behavior. Below the KCl line, ionicity decreases as a result of increased ion interactions. At a solvent-to-salt ratio of 30 : 1 to 8 : 1, the linear curve of the THF–KFSI electrolyte solutions indicates that the increase in K^+ concentration does not affect the Stokes radius of the K^+ and FSI^- ions. From a solvent-to-salt ratio of 7 : 1, the slope of the curve of the THF–KFSI electrolyte solutions changes, indicating a change of the Stokes radius of the K^+ and FSI^- ions. The non-linearity shown for the MeTHF–KFSI electrolyte solutions suggests that the increase in K^+ concentration affects the Stokes radius of the K^+ and FSI^- ions.

3.2. Solvation study of THF/MeTHF–KFSI electrolyte solutions

To understand the origin of the difference in the physicochemical properties from a fundamental solvation perspective, binary mixtures consisting of KFSI in THF and MeTHF at solvent-to-KFSI mole ratios of 10 : 1, 4 : 1 and 3 : 1 (only for THF), were investigated using Raman spectroscopy, ^{19}F NMR and ^{39}K NMR spectroscopy to probe the K^+–FSI^- and solvent–K^+ interactions. Theoretical calculations such as molecular dynamics (MD) and radial distribution functions (RDFs) can also help to interpret the experimentally observed data. Several possible solvate species can be defined, depending on the number of anions in the primary coordination shell around the K^+ cations. SSIPs are formed when the K^+ cations are completely separated from the counter anions by a layer of solvent molecules in the primary coordination shell. CIPs are formed when one anion is directly coordinated to a solvated K^+ cation, resulting in a neutral complex. The FSI^- anion can coordinate in a monodentate or a bidentate manner, depending on the coordination of the anion. AGGs form a large polymeric coordination network consisting of several K^+ cations linked together by two or three anions.

As shown in Fig. 1a, in the Raman spectra, the peak in the region between 650 cm^{-1} and 790 cm^{-1} can be assigned to the S–N stretching modes (ν(SN)) of the FSI^- anion, which is sensitive to its coordination environment.[45,46] The ν(SN) bands of THF–KFSI 10 : 1 and MeTHF–KFSI 10 : 1 are located at approximately 730 cm^{-1} and 736 cm^{-1}, respectively. For both THF–KFSI 3 : 1 and MeTHF–KFSI 4 : 1, the ν(SN) bands are located at approximately 738 cm^{-1}, while the ν(SN) band for THF–KFSI 4 : 1 is located at approximately 735 cm^{-1}. Upon increasing the KFSI concentration, the ν(SN) bands shift towards higher wavenumbers, indicating the enhanced formation of CIPs and AGGs. The ν(SN) band of MeTHF–KFSI 10 : 1 has already shifted significantly to higher wavenumbers compared to THF–KFSI 10 : 1. The same trend is observed in the binary mixtures at a solvent-to-salt ratio of 4 : 1, where the K^+ concentration is higher in THF (2.38 mol L^{-1}) than in MeTHF

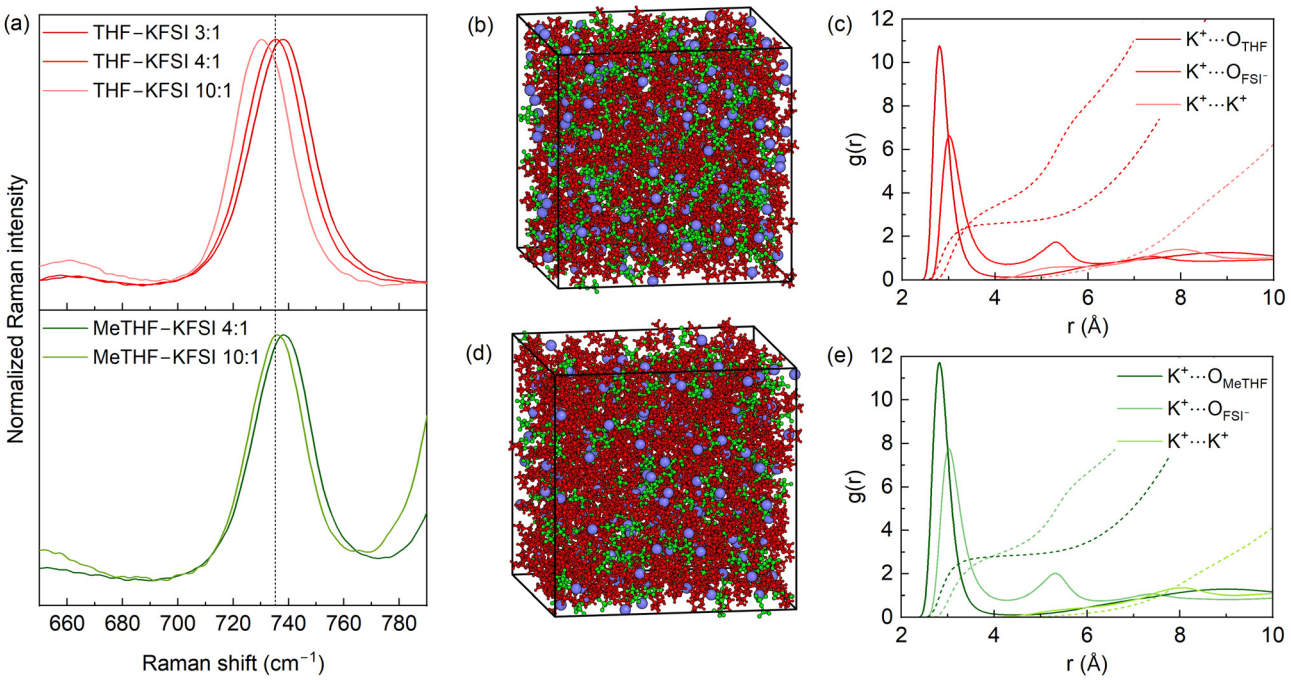

Fig. 1 (a) Raman spectra of the concentration dependence of the THF/MeTHF–KFSI binary mixtures in the range of 650 cm^{-1} to 770 cm^{-1}. MD simulation snapshots of the (b) THF–KFSI 3 : 1 and (d) MeTHF–KFSI 4 : 1 systems. The K^+ cation, FSI^- anion and solvent molecules (THF or MeTHF) are represented by the colors blue, green and red, respectively. RDFs (solid lines) and number integrals (dashed lines) of the K^+ cation interacting with the oxygen atoms of the solvent molecules and the FSI^- anions in (c) THF–KFSI 3 : 1 and (e) MeTHF–KFSI 4 : 1.

(2.02 mol L^{-1}). This suggests that CIPs and AGGs are already being formed in MeTHF–KFSI mixtures even under relatively diluted conditions. This trend can explain the substantial difference in ionic conductivity between the THF/MeTHF–KFSI binary mixtures. The methyl group in MeTHF increases the bulkiness of the solvent, preventing the K^+ cations from approaching the ethereal oxygen atom. This reduces the K^+–solvent interactions, hinders close packing around K^+, and reduces the coordination number. At the same KFSI concentration, the interactions between the K^+ cations and the FSI^- anions are therefore enhanced in MeTHF compared to THF. The Raman results demonstrate that MeTHF is a weaker donor solvent than THF, favoring the formation of anion-rich solvation structures (CIPs and AGGs) even under relatively diluted conditions.

The solvation structures of the THF/MeTHF–KFSI binary mixtures were also studied by NMR spectroscopy. The ^{1}H NMR spectra of pure THF and pure MeTHF are both in good agreement with the literature as depicted in Fig. S2a.[47,48] The ^{1}H NMR spectrum of pure THF was characterized by a multiplet at 1.98 ppm related to the two β-methylene groups, and a multiplet at 3.82 ppm corresponding to the two α-methylene groups (Fig. S2b). To make the assignment of the different proton environments in MeTHF easier to understand, eight different proton environments have been randomly designated ''A'' through ''H'', which indicate the highest-to-lowest chemical shift in MeTHF (Fig. S2c). For instance, protons ''A'' and ''B'' correspond to the methylene group closest to the ethereal oxygen, which is assigned to the highest chemical shift at 4.04 ppm. Proton ''C'' is related to the methine group, which is characterized by a multiplet at 3.82 ppm. Proton ''D'' represents the methyl group, which is characterized by a doublet at 1.38 ppm. The protons ''E'', ''F'', ''G'', and ''H'' correspond to the other two methylene groups. Upon solvation of KFSI, the NMR signals shift upfield, indicating the shielding effect on all ^{1}H nuclei. The addition of KFSI to MeTHF causes the multiplet at 4.04 ppm to split into two different multiplets, which indicates that upon solvation, proton ''B'' will be closer to the K^+ cation than proton ''A''. As the K^+ concentration increases, the distance between these multiplets also increases. As shown in Fig. S3a, for the THF–KFSI mixtures, upon increasing the KFSI concentration, the ^{19}F NMR signal of the FSI^- anion is more deshielded (higher chemical shifts). The higher ^{19}F chemical shift could result from the reduced electron density in the FSI^- anions, possibly indicating an enhanced K^+–FSI^- ion pairing. For both MeTHF–KFSI 10 : 1 and MeTHF–KFSI 4 : 1, the ^{19}F NMR signal of the FSI^- anions is located at exactly the same chemical shift, indicating that CIPs and AGGs are already being formed in MeTHF–KFSI mixtures even under relatively diluted conditions. This observation confirms the results obtained by Raman spectroscopy. When increasing the KFSI concentration, the ^{39}K signal is more shielded (lower chemical shifts), as shown in Fig. S3b. The lower ^{39}K chemical shift arises from the increased electron density around the K^+ ions, as a result of a stronger ion solvation or an increased K^+–FSI^- ion pairing. However, in general, the MeTHF–KFSI mixtures show higher ^{39}K chemical shifts than the THF–KFSI mixtures, while the Raman and ^{19}F NMR data show that the K^+ cations receive more electron contribution from the FSI^- anions in MeTHF than in THF. Taken together with ^{1}H NMR and Raman spectra discussed above, these trends are consistent with ^{19}F and ^{39}K chemical shifts being dominated by local diamagnetic effects resulting from electron density transfer from THF/MeTHF to the K^+ ions upon solvation.

MD simulations were performed to investigate the cation's solvation environment (Fig. 1b and d). The simulated systems comprise the THF–KFSI 3 : 1 and the MeTHF–KFSI 4 : 1 electrolyte solution. RDFs were computed to analyze the cation's interactions with the different species present in the system. For the ease of comparison with the solvent, the discussion of the cation's interaction with the anion will be largely limited to the anion's oxygen atoms. Fig. 1c and e show the RDFs for the cation's interactions with the oxygen atoms of the FSI^- anion and the solvent in the two electrolyte solutions. While their relative height differs by system, the peak positions and the minima are largely consistent across both electrolyte solutions. Sharp peaks are observed for either interaction in both systems at distances of 2.80 Å and 3.02 Å for the solvent and anion, respectively, indicating an ordered first coordination shell and strong ion association. The number integrals at the first minimum of the cation–anion and cation–solvent RDFs, which correspond to the average coordination number in the first solvation shell, are 3.69 and 2.63 in THF–KFSI 3 : 1 and 3.05 and 2.84 in MeTHF–KFSI 4 : 1, respectively, indicating a higher prevalence of ion pairing and aggregate formation in THF–KFSI 3 : 1. At larger distances, two smaller peaks are observed for the anion's oxygen atoms located at 5.32 Å and 7.38 Å. These correspond to the non-coordinating oxygen atoms of a coordinating anion and an anion in the second solvation shell. A shallow and broad second-shell peak is observed in either system for the cation's interaction with the solvent's oxygen atoms at 9.00 Å, indicating no ordered aggregation of solvent molecules around the cation beyond the first solvation shell. For the cation–cation interaction, a small peak is observed at 8.04 Å as well as a shoulder around 5.40 Å in both electrolyte solutions. Relative to the main peak, this shoulder is more pronounced in THF–KFSI 3 : 1 than in MeTHF–KFSI 4 : 1, further indicating the stronger prevalence of aggregate formation in the former system.

The RDFs show that ion association is prevalent in both electrolyte solutions. To obtain a more detailed picture of the composition and configuration of the cation's first solvation shell, neighbor count analyses were performed. An oxygen atom is considered part of the first solvation shell if it is within 4.28 Å for the anion and 4.38 Å for the solvent, corresponding to the locations of the first minima in their respective RDFs (Fig. 1c and e). Evaluating these conditions for every cation over the simulation trajectory yields histograms of the fraction of cations coordinated by a given number of particles. These histograms are shown in Fig. S4a and b (for the anion-centric neighbor counts, see Fig. S6). In both electrolyte solutions, the most common coordination motif is a cation coordinated by

three solvent molecules and three anion oxygen atoms. However, compared to MeTHF–KFSI 4 : 1, the distribution in THF–KFSI 3 : 1 is shifted toward smaller solvent neighbor counts and larger anion neighbor counts. Consistent with the RDFs, the THF–KFSI 3 : 1 electrolyte solution shows a stronger tendency for aggregate formation, with 89% of anions coordinating two or more cations in THF–KFSI 3 : 1 *versus* 78% in MeTHF–KFSI 4 : 1. A small but non-negligible fraction of cations, 0.8% in THF–KFSI 3 : 1 and 1.5% in MeTHF–KFSI 4 : 1, are fully coordinated by solvent molecules and share no direct contacts with any anion. Counting both the anion and solvent oxygen atoms, the total coordination numbers are 6.3 in THF–KFSI 3 : 1 and 5.9 in MeTHF–KFSI 4 : 1, suggesting a denser coordination shell in THF–KFSI 3 : 1.

The FSI^- anion may coordinate the cation in several distinct configurations. The most prominent motifs are the monodentate and bidentate coordination *via* its oxygen atoms. The ratio of monodentate to bidentate coordination remains nearly constant across systems with 56 : 44 in THF–KFSI 3 : 1 and 54 : 46 in MeTHF–KFSI 4 : 1. Based on these results, the most common coordination motif for the cation in both electrolyte solutions is one where it is coordinated by three solvent molecules and three anion oxygen atoms donated by two anions, one binding in a monodentate and the other in a bidentate way.

In addition to its oxygen atoms, the FSI^- anion's central nitrogen and fluorine atoms may also act as adjacent or direct coordination sites. The percentage of cations sharing a contact with the nitrogen atom of an anion was determined to be 30% in THF–KFSI 3 : 1 and 24% in MeTHF–KFSI 4 : 1, respectively, mainly shared with a coordinating oxygen of the same anion. Interestingly, the difference in fluorine contacts is more pronounced with 44% of cations in THF–KFSI 3 : 1 and 26% in MeTHF–KFSI 4 : 1 sharing a contact with an anion's fluorine atom adjacent to a coordinating oxygen atom. In comparison, the direct coordination through fluorine with no adjacent oxygen contact is less prevalent, being shared by 7% of cations in THF–KFSI 3 : 1 and 3% in MeTHF–KFSI 4 : 1.

The Raman analysis shows that, at the same solvent-to-salt ratio (where the K^+ concentration in THF is even slightly higher than that in MeTHF), more anion-rich solvation structures (CIPs and AGGs) are formed in MeTHF than in THF. In contrast, the MD simulations indicate stronger aggregation in THF–KFSI 3 : 1 than in MeTHF–KFSI 4 : 1. This is likely due to the higher K^+ concentration in THF–KFSI 3 : 1. Since the K^+ concentration in THF–KFSI 3 : 1 (2.94 mol L^{-1}) is significantly higher than in MeTHF–KFSI 4 : 1 (2.02 mol L^{-1}), it is highly likely that this solvent effect of MeTHF is negated by the higher solubility of KFSI in THF.

3.3. Electrochemical stability of THF/MeTHF–KFSI binary mixtures towards potassium metal

The plating and stripping behavior of potassium metal in both electrolyte solutions was investigated by cyclic voltammetry. As shown in Fig. 2a and b, in the negative scan direction, an abrupt negative current density was observed at a potential of approximately −0.05 V *vs.* K^+/K. This reduction corresponds to

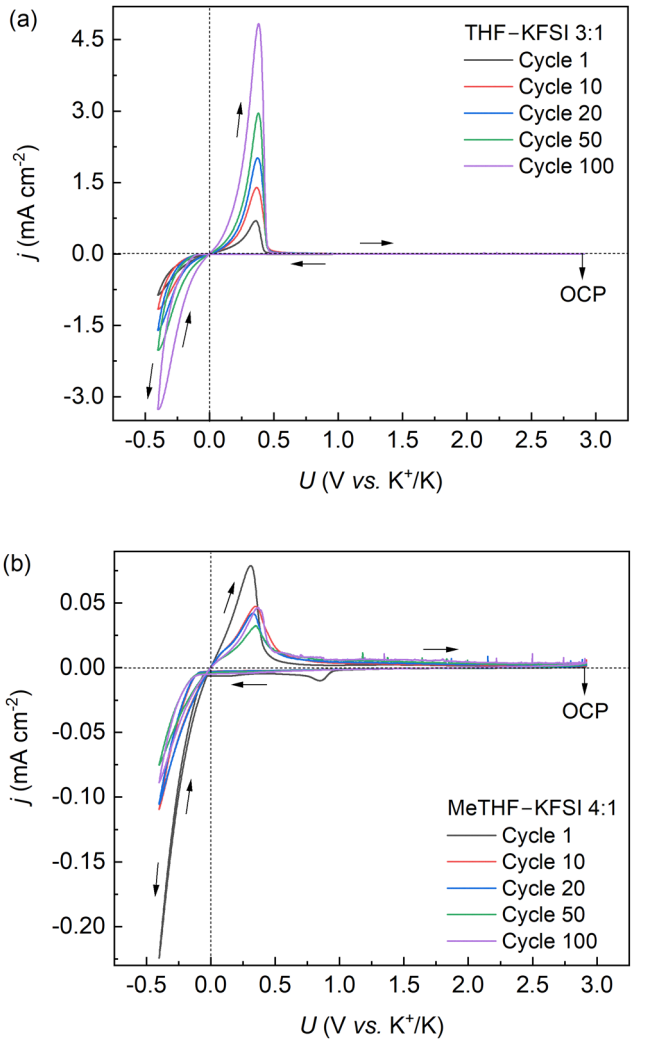

Fig. 2 Cyclic voltammograms recorded in K‖Al half-cells using aluminum foil as the working electrode and a potassium metal chip as the counter electrode and pseudo-reference electrode at a scan rate of 1 mV s^{-1} at ~25 °C with (a) THF–KFSI 3 : 1 and (b) MeTHF–KFSI 4 : 1.

the bulk deposition of potassium metal, which was supported by the presence of a nucleation loop. During the reverse scan, the deposited potassium metal starts to strip from approximately 0.0 V *vs.* K^+/K, indicating that no severe blocking has occurred within the scanned window, followed by a characteristic stripping peak. For the THF–KFSI 3 : 1 electrolyte solution, the plating and stripping peaks increased with the number of scans. In contrast, for the MeTHF–KFSI 4 : 1 electrolyte solution, the plating and stripping peaks became smaller as the number of scans increased. In addition, during the reverse scan of the MeTHF–KFSI 4 : 1 electrolyte solution, some noise was observed at positive potentials, which may be due to the presence of unstripped potassium metal. The current densities achieved during cycling using MeTHF–KFSI 4 : 1 are an order of magnitude lower compared to the cycling of THF–KFSI 3 : 1, which can be explained by the lower ionic conductivity of the electrolyte solution.

In addition, galvanostatic cycling experiments were performed in K‖Al half-cells to evaluate the reversibility of the

plating and stripping of potassium metal in the THF/MeTHF–KFSI binary mixtures. For each cycle, CE is defined by the ratio of potassium plating capacity to potassium stripping capacity. Different current densities of 0.5, 1.0, 2.0 and 4.0 mA cm^{-2} were used for cycling with a cutoff capacity of 1 mAh cm^{-2}. Two coin cells were prepared for each set of cycling conditions (see Table S4.). The cycling data shown in the graphs are representative. Fig. 3a and b show the galvanostatic discharge/charge curves and the cycling performance using the THF/MeTHF–KFSI binary mixtures in K‖Al half-cell configuration. At a current density of 0.5 mA cm^{-2}, the K‖Al cell with THF–KFSI 3 : 1 exhibited a significantly higher initial CE (95.4%) compared to MeTHF–KFSI 4 : 1 (88.7%). In the first 3 to 7 cycles, the CE was below 98% due to the initial side reactions between the electrolyte solutions and the highly reactive potassium metal. In the subsequent cycles, CE continued to increase, eventually reaching ~99%. The continuous consumption of the electrolyte solution was prevented by the formation of an SEI. Despite the fact that the initial CE is lower for the MeTHF–KFSI 4 : 1 electrolyte solution, it achieved the same stable CE of ~99% in fewer cycles compared to the THF–KFSI 3 : 1 electrolyte solution. Both THF–KFSI 3 : 1 and MeTHF–KFSI 4 : 1 enabled reversible potassium plating and stripping in long-term cycling at a current density of 0.5 mA cm^{-2}, achieving a high CE of ~99% over 500 cycles. The CE of THF–KFSI 3 : 1 fluctuates more compared to MeTHF–KFSI 4 : 1. As shown in Fig. 3a and b, the initial nucleation overpotential ($\eta_{nucl.}$) of the K‖Al half-cells using THF–KFSI 3 : 1 was significantly lower (~0.150 V) compared to MeTHF–KFSI 4 : 1 (~0.236 V), which is due to the higher ionic conductivity of THF–KFSI 3 : 1. The polarization remained nearly unchanged within 400 cycles as shown in Fig. 3a, indicating that a stable SEI was readily established at early stages for THF–KFSI 3 : 1. As the current density increased from 0.5 to 4 mA cm^{-2}, the K‖Al half-cells with THF–KFSI 3 : 1 displayed some polarization increases of ~0.142, ~0.196, ~0.249 and ~0.327 V (Fig. S7a), demonstrating

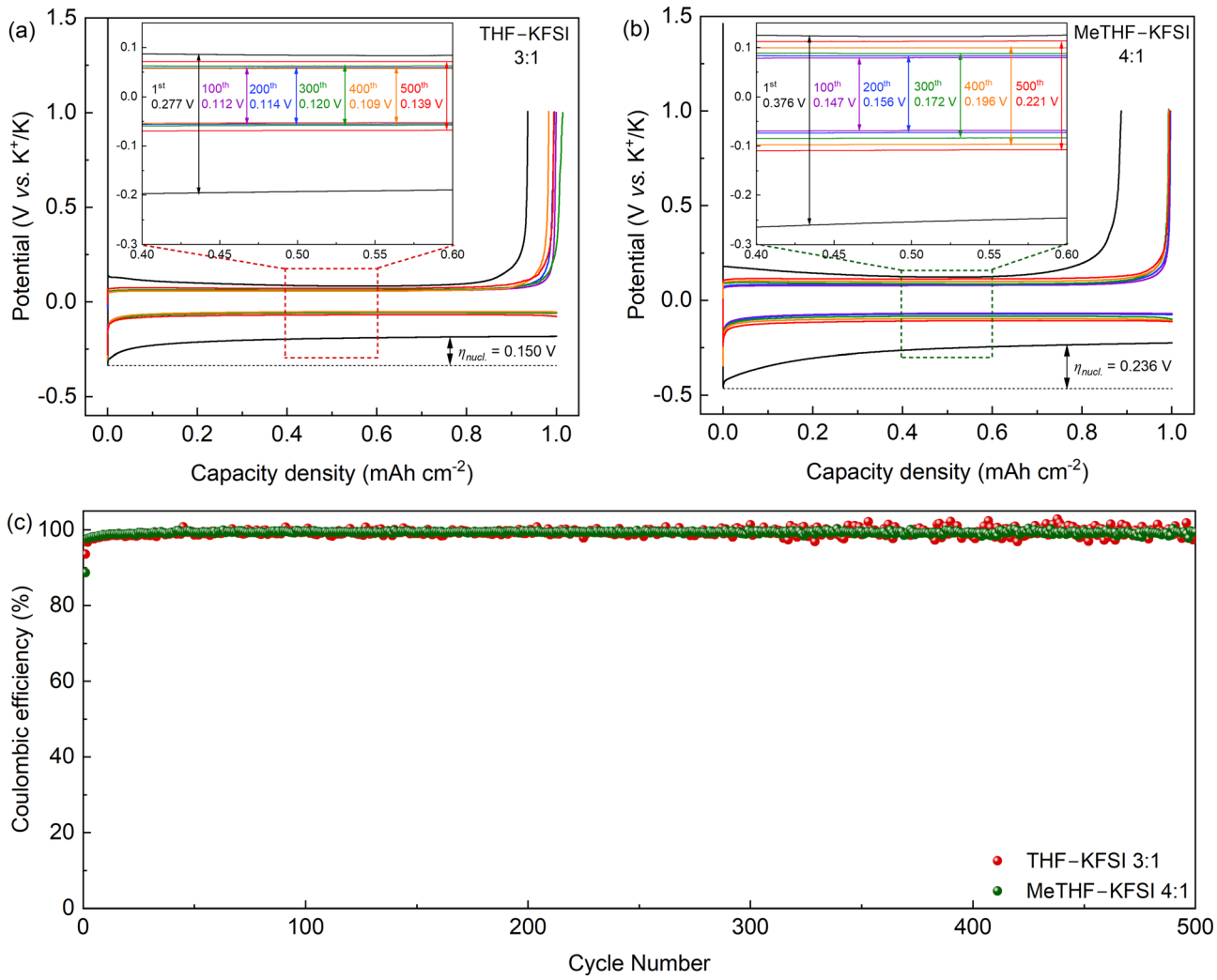

Fig. 3 Potassium metal plating/stripping behavior in THF/MeTHF–KFSI electrolyte solutions. Galvanostatic potassium metal plating/stripping profiles of K‖Al half-cells cycled in (a) THF–KFSI 3 : 1 and in (b) MeTHF–KFSI 4 : 1 at a current density of 0.5 mA cm^{-2} with a cutoff capacity of 1 mAh cm^{-2}. (c) Potassium metal plating/stripping CE of K‖Al half-cells cycled in different electrolyte solutions at a current density of 0.5 mA cm^{-2} with a cutoff capacity of 1 mAh cm^{-2}.

relatively good rate capability. However, the K‖Al half-cells with MeTHF–KFSI 4 : 1 displayed polarization increases of ~0.188, ~0.274, ~0.346 and ~0.422 V (Fig. S7b).

When tested at a high current density of 4.0 mA cm^{-2}, the K‖Al half-cell with MeTHF–KFSI 4 : 1 was found to exhibit poor long-term cycling stability with the CE already decreasing significantly after 35 cycles (Fig. S7c). A longer cycle life of more than 100 cycles with an average CE of ~98% was achieved with THF–KFSI 3 : 1 using the same cycling conditions. Overall, at higher current densities, the long-term cycling stability of THF–KFSI 3 : 1 was better than that of MeTHF–KFSI 4 : 1, possibly due to the higher KFSI concentration, which reduces the number of free solvent molecules available for reduction by the potassium metal.

3.4. Morphological and structural characterization of the potassium metal electrode

The reversibility of the potassium plating/stripping is determined by the surface morphology of the potassium metal and the composition of the SEI. X-ray diffraction (XRD), scanning electron microscopy (SEM), energy dispersive X-ray spectroscopy (EDX) and X-ray photoelectron spectroscopy (XPS) were applied to investigate the electrodeposition of the potassium metal.

As shown in Fig. S8, the XRD pattern of the potassium metal chip (99.7%) exhibits two diffraction peaks, which are ascribed to (110) and (200), respectively, confirming the body-centered cubic structure.[49,50] The XRD pattern of the deposited potassium metal on the aluminum current collector exhibits a strong preference for the (110) orientation, while the diffraction peak for the (200) plane is not observed.

Fig. 4a–d show the surface morphology of the deposited potassium metal on the aluminum current collector during the first cycle at a current density of 0.5 mA cm^{-2} and a capacity density of 1 mAh cm^{-2}. For both electrolyte solutions, the electrochemically deposited potassium metal displayed an uneven and nonuniform morphology on the aluminum substrate. Only parts of the aluminum substrate were covered with numerous irregularly shaped potassium metal structures, but no dendritic structures were observed. As shown in Fig. 4d, the deposited potassium metal in MeTHF–KFSI 4 : 1 contains larger dents in the potassium metal compared to THF–KFSI 3 : 1. This may explain the lower CE during the first cycle of MeTHF–KFSI 4 : 1, as the increase in surface area can induce more excessive side reactions with the electrolyte solution. The 'sponge'-like morphology should maintain a dendrite-free potassium metal electrode upon cycling, which is less likely to puncture the separator.

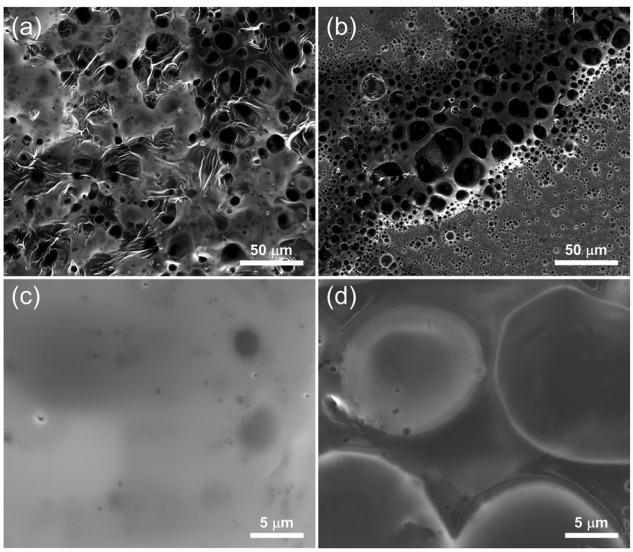

Fig. 4 SEM images of the deposited potassium metal on the aluminum current collector after discharging of the first cycle at 0.5 mA cm^{-2} under 1 mAh cm^{-2} (a) and (c) in THF–KFSI 3 : 1 and (b) and (d) in MeTHF–KFSI 4 : 1.

Furthermore, the SEM image of the cross-section (Fig. S9a) revealed that the thickness of the deposited potassium metal is approximately three times greater than the thickness of the aluminum current collector. During the sample preparation for SEM-EDX analysis, exposure to air could not be avoided, resulting in a signal in the EDX spectrum for oxygen (Fig. S9c).

To gain a deeper insight into the interfacial reactions occurring between the highly reactive potassium metal and the electrolyte solutions, X-ray photoelectron spectroscopy (XPS) was employed to systematically examine the chemical composition and structural characteristics of the solid–electrolyte interphase (SEI) formed on the aluminum current collector during the plating and stripping processes of potassium metal. Understanding the SEI composition is essential, as it plays a critical role in stabilizing the electrode–electrolyte interface, mitigating parasitic reactions, and influencing the reversibility of potassium metal plating and stripping.

As illustrated in Fig. 5a–d, the SEI layers generated in THF–KFSI 3 : 1 and MeTHF–KFSI 4 : 1 electrolyte solutions exhibit broadly similar chemical compositions, suggesting comparable interfacial decomposition pathways in both systems.

The C 1s spectra reveal multiple characteristic peaks corresponding to C–C/C–H (284.8 eV), C–OH/C–O–C (286.3 eV), CO_3^{2-} (288.2 eV), and a weak O–C═O (288.8 eV) feature.[51–53] These carbonaceous species are primarily attributed to solvent decomposition and the subsequent formation of organic and inorganic carbonate fragments. The coexistence of these functional groups indicates partial oxidative degradation of the ether-based solvents during the electrochemical cycling of potassium metal.

In the O 1s spectra, signals at binding energies of 530.4 eV ($R–O^-$), 531.4 eV (C═O), 532.45 eV (S═O), and 533.1 eV (C–OH/C–O–C) are observed.[52–55] These oxygen-containing components are likely derived from both the decomposition of the solvent molecules and the anionic species of the salt (FSI^-). The detection of multiple oxygen environments implies a heterogeneous SEI structure containing both organic moieties and inorganic oxygenated compounds.

The F 1s spectra exhibit two fluorine-containing environments located at 686.4 eV and 684.7 eV, which can be assigned to S–F and F^- species, respectively.[51] The appearance of the F^- component suggests cleavage of the S–F bond in the FSI^- anion during interfacial reactions, leading to the formation of inorganic fluoride species within the SEI.

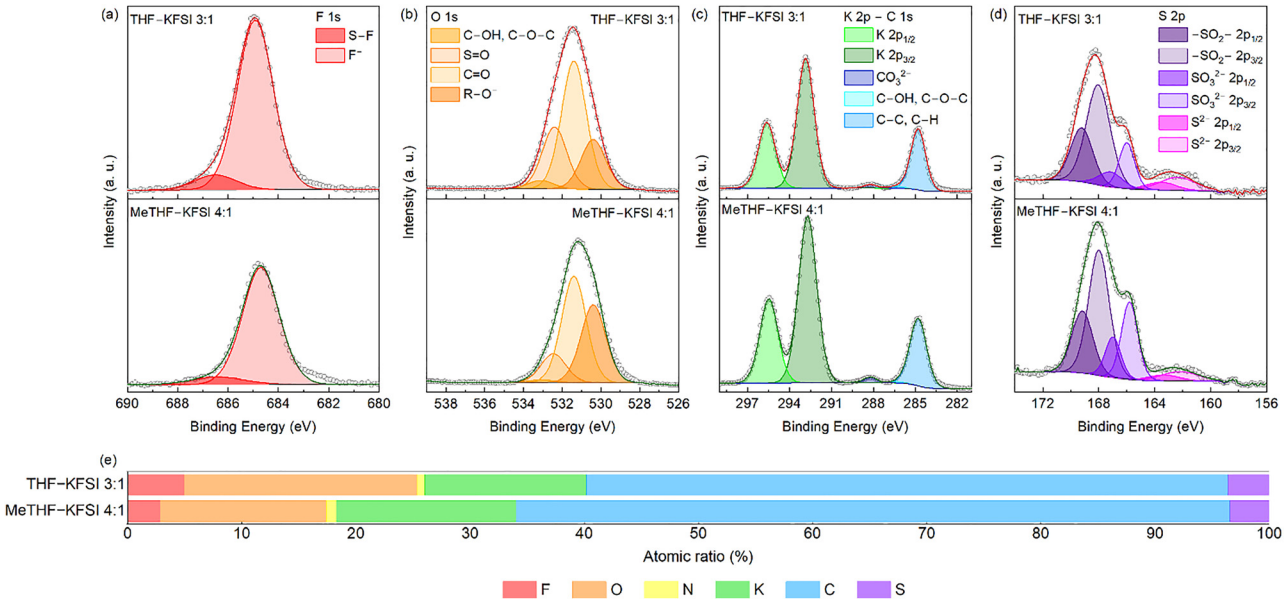

Fig. 5 XPS spectra of the SEI layers formed on the aluminum current collector after the first cycle: (a) F 1s, (b) O 1s, (c) K 2p–C 1s and (d) S 2p. (e) The atomic ratio of the SEI layers formed on the aluminum current collector after the first cycle in THF–KFSI 3 : 1 and MeTHF–KFSI 4 : 1.

Furthermore, the S 2p spectra confirm the presence of sulfur-containing species such as SO_2, SO_3^{2-}, and S^{2-}, which are attributed to the decomposition of the $-SO_2-$ functional group in the FSI^- anion.[56,57] The coexistence of oxidized (SO_2/SO_3^{2-}) and reduced (S^{2-}) sulfur species suggests a complex redox environment at the interface, driven by the strong reducing nature of metallic potassium.

Elemental analysis (Fig. 5e) shows that the SEI formed in the THF–KFSI 3 : 1 electrolyte solution contains a higher relative fluorine content, suggesting a greater extent of FSI^--derived decomposition products compared to MeTHF–KFSI 4 : 1. In contrast, the MeTHF-based system exhibits a higher carbon content, while sulfur and nitrogen contents remain broadly comparable between the two electrolyte solutions. In addition, the O 1s spectra indicate a lower relative oxygen content in the SEI formed with MeTHF–KFSI 4 : 1, suggesting differences in the distribution of oxygen-containing species within the interphase.

The solvation structure determines the SEI chemistry, as the species closest to the potassium metal surface are reduced first. The SEI layers formed in both electrolyte systems display largely similar chemical compositions, indicating analogous interfacial decomposition pathways. Overall, these findings indicate that both solvent and anion decomposition contribute significantly to SEI formation, leading to a mixed organic–inorganic interphase that governs the electrochemical stability of potassium metal electrodes. The higher KF content in the SEI for THF–KFSI 3 : 1 is most likely due to the significantly higher K^+ concentration in THF–KFSI 3 : 1 than in MeTHF–KFSI 4 : 1. Although the XPS data indicate the presence of KF, which clearly originates from the decomposition of the anion, a correlation to cycling performance cannot be established. Previous studies on lithium anode-free and lithium metal batteries have shown that there is a clear link between fluorine-rich SEI components and cyclability (such as dendrite suppression and improved cation conductivity). Further research is therefore needed to confirm the correlation between KF-rich SEIs and higher cycling performance.

3.5. Cycling of THF–KFSI 3:1 and MeTHF–KFSI 4:1 on organic cathodes

K_2-Co-benzene-1,2,4,5-tetra-methylsulfonamide (K_2-Co-PTtSA) was chosen as the cathode material due to its high working redox potential (~3.25 V *vs.* K^+/K) and excellent cycling performance. In addition, sulfonamide coordination polymers are, to date, the only class of materials synthesized directly in a K-containing phase, in a manner analogous to conventional Li-ion cathodes.[33,58] To compare the electrochemical performance under different electrolyte conditions, the K_2-Co-PTtSA electrode was tested in a two-electrode coin-cell configuration using potassium metal as both the counter and reference electrodes, with two electrolyte formulations: THF–KFSI 3 : 1 and MeTHF–KFSI 4 : 1.

The galvanostatic charge–discharge profiles (Fig. 6a and b) are similar in both cases, exhibiting two well-defined plateaus corresponding to the stepwise two-electron redox process of the $PTtSA^{4-}$ ligand. The THF-based electrolyte solution exhibits higher active-material utilization compared to MeTHF, delivering discharge capacities of ~80 mAh g^{-1} and ~72 mAh g^{-1}, respectively, relative to a theoretical capacity of 94 mAh g^{-1}.

When evaluated at increasing current densities, both electrolyte systems show a similar decrease in energy density, with only minor differences in discharge capacity. At 10C, capacity retention remains comparable, reaching 63% of the initial capacity for the THF electrolyte and 64% for MeTHF. In contrast, pronounced differences emerge during long-term cycling (Fig. 6c), where the MeTHF-based electrolyte exhibits

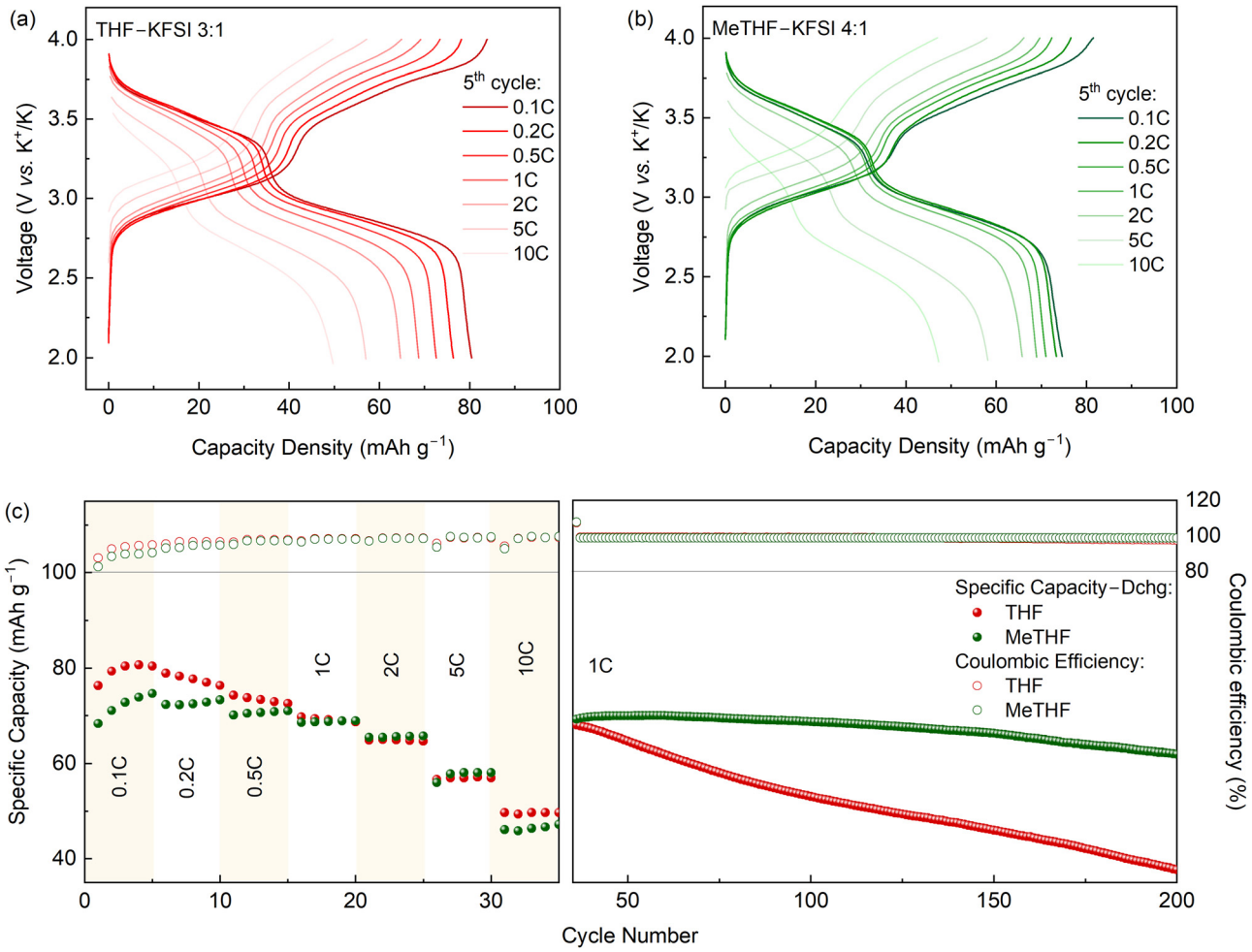

Fig. 6 Electrochemical performances of KMBs using K_2-Co-PTtSA as a positive electrode material cycled in THF/MeTHF–KFSI binary mixtures. Galvanostatic charge–discharge profiles of the first five cycles of K‖K_2-Co-PTtSA cells cycled with (a) THF–KFSI 3 : 1 and (b) MeTHF–KFSI 4 : 1 at a rate of 0.1C (1C corresponds to 100 mA g^{-1}). (c) Rate and long-term cycling performance of K‖K_2-Co-PTtSA cells in THF–KFSI 3 : 1 and MeTHF–KFSI 4 : 1 at different cycling rates ranging from 0.1C to 10C.

significantly improved capacity retention compared to THF. Nevertheless, the CE remains above 99% in both systems. This behavior could possibly be explained by differences in cathode solubility in the two electrolyte solutions, although other factors may also contribute, such as wettability, ionic transport, or interfacial impedance at the cathode. Organic battery materials are known to be susceptible to dissolution in organic solvents, often leading to rapid capacity fading. Importantly, this solubilization process is strongly dependent on electrolyte composition. To confirm this hypothesis, the cathode material was further tested in a two-electrode configuration using AC as the counter electrode (Fig. S12). The same amount of electrolyte solution, separator type, and cathode loading were used as in the K‖K_2-Co-PTtSA cells, thereby eliminating any contribution from potassium metal and avoiding parasitic reactions associated with the potassium anode. The same trend was observed in these cells, indicating that the results are consistent with enhanced dissolution of K_2-Co-PTtSA in THF–KFSI 3 : 1, which may contribute to the accelerated capacity fading relative to MeTHF–KFSI 4 : 1.

4. Conclusions

A comparative analysis of two optimized electrolyte solutions was conducted using weakly coordinating solvents, namely THF–KFSI 3 : 1 and MeTHF–KFSI 4 : 1. Both electrolyte formulations enabled reversible potassium metal plating and stripping on the aluminum electrode at a high CE of ~99% for 500 cycles at 0.5 mA cm^{-2} and 1 mAh cm^{-2}. The K‖Al-half cells constructed using THF–KFSI 3 : 1 exhibit better performance with lower polarization over 500 cycles compared to MeTHF–KFSI 4 : 1. The more inorganic-rich SEI layer formed in THF–KFSI 3 : 1, attributed to the higher KFSI concentration in THF, may explain the improved electrochemical performance during the plating and stripping of potassium metal. The THF–KFSI 3 : 1 electrolyte solution has the most potential for use in anode-free metal batteries, as the cycling performance in the K‖Al cells was better compared to MeTHF–KFSI 4 : 1. As a proof of concept, the electrolyte solutions were cycled in a coin cell configuration with K_2-Co-PTtSA to demonstrate their compatibility with an organic cathode material. During long-term cycling,

MeTHF–KFSI 4 : 1 exhibited significantly improved capacity retention compared to THF–KFSI 3 : 1, which could possibly be explained by the higher solubility of K_2-Co-PTtSA in THF–KFSI 3 : 1, while the CE remained above 99% in both electrolyte solutions. In K‖K_2-Co-PTtSA cells, the greener MeTHF–KFSI 4 : 1 electrolyte solution was better in terms of cycling performance compared to its more harmful analogue THF–KFSI 3 : 1. The long-term cycling of THF–KFSI 3 : 1 could potentially be improved by selecting a cathode material with lower solubility in the electrolyte solution, but this is beyond the scope of this work. Overall, this study provides a comprehensive exploration of the electrochemical properties of cyclic ether-based electrolyte solutions in KMBs. In addition, the importance of probing the solvation structure and the interfacial chemistry through careful design of the electrolyte solution was highlighted.

Author contributions

Roy Heyns: investigation, methodology, formal analysis, and writing – original draft. Robert Markowski, Andrii Kachmar, Johannes Ingenmey and Wouter Monnens: review, methodology, and validation. Koen Binnemans, Alexandru Vlad, Barbara Kirchner and Jan Fransaer: review & editing, supervision, resources, project administration, methodology, and funding acquisition.

Conflicts of interest

There are no conflicts to declare.

Data availability

The authors confirm that the data supporting the findings of this study are available within the article and its supplementary information (SI). Supplementary information: Ionic conductivity/viscosity/density, NMR spectra, RDFs, Coulombic efficiencies, XRD diffractogram, EDX spectrum, and XPS profiles. See DOI: https://doi.org/10.1039/d6ya00089d.

Acknowledgements

This work was supported by the FWO and F.R.S-FNRS project ECOBAT (40007515) under the Excellence of Science (EOS) program and through infrastructure grant I002720N. Special thanks go to Gert Steurs, Stijn Raiguel and Pieter Geysens for performing the NMR measurements and providing valuable insights regarding the solvation analysis.

Notes and references

1 N. Nitta, F. Wu, J. T. Lee and G. Yushin, *Mater. Today*, 2015, **18**, 252–264.
2 V. Anoopkumar, B. John and T. D. Mercy, *ACS Appl. Energy Mater.*, 2020, **3**, 9478–9492.
3 A. Eftekhari, Z. Jian and X. Ji, *ACS Appl. Mater. Interfaces*, 2017, **9**, 4404–4419.
4 N. Yabuuchi, K. Kubota, M. Dahbi and S. Komaba, *Chem. Rev.*, 2014, **114**, 11636–11682.
5 T. Hosaka, K. Kubota, A. S. Hameed and S. Komaba, *Chem. Rev.*, 2020, **120**, 6358–6466.
6 W. Xu, H. Wang, Y. Gao, Y. Wei, H. Zhang, C. Gao, F. Kang and D. Zhai, *Energy Adv.*, 2022, **1**, 191–196.
7 K. Kubota, M. Dahbi, T. Hosaka, S. Kumakura and S. Komaba, *Chem. Rec.*, 2018, **18**, 459–479.
8 X. Wu, D. P. Leonard and X. Ji, *Chem. Mater.*, 2017, **29**, 5031–5042.
9 Q. Yao and C. Zhu, *Adv. Funct. Mater.*, 2020, **30**, 2005209.
10 A. Eftekhari, *J. Power Sources*, 2004, **126**, 221–228.
11 M. Okoshi, Y. Yamada, S. Komaba, A. Yamada and H. Nakai, *J. Electrochem. Soc.*, 2017, **164**, A54–A60.
12 S. Komaba, T. Hasegawa, M. Dahbi and K. Kubota, *Electrochem. Commun.*, 2015, **60**, 172–175.
13 Z. Wang, S. M. Selbach and T. Grande, *RSC Adv.*, 2014, **4**, 3973–3983.
14 D. Petersen, M. Gronenberg, G. Lener, E. P. M. Leiva, G. L. Luque, S. Rostami, A. Paolella, B. J. Hwang, R. Adelung and M. Abdollahifar, *Mater. Horiz.*, 2024, **11**, 5914–5945.
15 Y. Lei, L. Qin, R. Liu, K. C. Lau, Y. Wu, D. Zhai, B. Li and F. Kang, *ACS Appl. Energy Mater.*, 2018, **1**, 1828–1833.
16 N. S. Katorova, S. S. Fedotov, D. P. Rupasov, N. D. Luchinin, B. Delattre, Y.-M. Chiang, A. M. Abakumov and K. J. Stevenson, *ACS Appl. Energy Mater.*, 2019, **2**, 6051–6059.
17 J. Zhang, Z. Cao, L. Zhou, G.-T. Park, L. Cavallo, L. Wang, H. N. Alshareef, Y.-K. Sun and J. Ming, *ACS Energy Lett.*, 2020, **5**, 3124–3131.
18 J. Sun, Y. Du, Y. Liu, D. Yan, X. Li, D. H. Kim, Z. Lin and X. Zhou, *Chem. Soc. Rev.*, 2025, **54**, 2543–2594.
19 C. Jo and S. Myung, *Adv. Energy Mater.*, 2024, **14**, 2400217.
20 G. Jiang, F. Li, H. Wang, M. Wu, S. Qi, X. Liu, S. Yang and J. Ma, *Small Struct.*, 2021, **2**, 2000122.
21 Y. Yamada, K. Furukawa, K. Sodeyama, K. Kikuchi, M. Yaegashi, Y. Tateyama and A. Yamada, *J. Am. Chem. Soc.*, 2014, **136**, 5039–5046.
22 Y. Yamada, K. Usui, C. H. Chiang, K. Kikuchi, K. Furukawa and A. Yamada, *ACS Appl. Mater. Interfaces*, 2014, **6**, 10892–10899.
23 M. Nie, D. P. Abraham, D. M. Seo, Y. Chen, A. Bose and B. L. Lucht, *J. Phys. Chem. C*, 2013, **117**, 25381–25389.
24 Y. Yamada and A. Yamada, *J. Electrochem. Soc.*, 2015, **162**, A2406–A2423.
25 N. Xiao, W. D. McCulloch and Y. Wu, *J. Am. Chem. Soc.*, 2017, **139**, 9475–9478.
26 T. Hosaka, T. Matsuyama, K. Kubota, R. Tatara and S. Komaba, *J. Mater. Chem. A*, 2020, **8**, 23766–23771.
27 W. Xu, H. Wang, J. Hu, H. Zhang, B. Zhang, F. Kang and D. Zhai, *Chem. Commun.*, 2021, **57**, 1034–1037.
28 A. Choi, Z. Li, Y. Zhang, H. Wang and V. G. Pol, *J. Electrochem. Soc.*, 2025, **172**, 110526.
29 V. Pace, P. Hoyos, L. Castoldi, P. Domínguez de María and A. R. Alcántara, *ChemSusChem*, 2012, **5**, 1369–1379.

30 A. Corma, S. Iborra and A. Velty, *Chem. Rev.*, 2007, **107**, 2411–2502.
31 X. He, N. Iqbal, U. Ghani and T. Li, *J. Alloys Compd.*, 2024, **981**, 173680.
32 P. K. Nayak, L. Yang, W. Brehm and P. Adelhelm, *Angew. Chem., Int. Ed.*, 2018, **57**, 102–120.
33 J. Wang, X. Guo, P. Apostol, X. Liu, K. Robeyns, L. Gence, C. Morari, J.-F. Gohy and A. Vlad, *Energy Environ. Sci.*, 2022, **15**, 3923–3932.
34 A. P. Thompson, H. M. Aktulga, R. Berger, D. S. Bolintineanu, W. M. Brown, P. S. Crozier, P. J. In'T Veld, A. Kohlmeyer, S. G. Moore, T. D. Nguyen, R. Shan, M. J. Stevens, J. Tranchida, C. Trott and S. J. Plimpton, *Comput. Phys. Commun.*, 2022, **271**, 108171.
35 W. L. Jorgensen, D. S. Maxwell and J. Tirado-Rives, *J. Am. Chem. Soc.*, 1996, **118**, 11225–11236.
36 K. P. Jensen and W. L. Jorgensen, *J. Chem. Theory Comput.*, 2006, **2**, 1499–1509.
37 J. N. Canongia Lopes and A. A. H. Pádua, *J. Phys. Chem. B*, 2004, **108**, 16893–16898.
38 L. Martínez, R. Andrade, E. G. Birgin and J. M. Martínez, *J. Comput. Chem.*, 2009, **30**, 2157–2164.
39 S. Nose, *J. Phys.: Condens. Matter*, 1990, **2**, SA115–SA119.
40 W. G. Hoover, H. A. Posch, B. L. Holian, M. J. Gillan, M. Mareschal and C. Massobrio, *Mol. Simul.*, 1987, **1**, 79–86.
41 M. Brehm and B. Kirchner, *J. Chem. Inf. Model.*, 2011, **51**, 2007–2023.
42 M. Brehm, M. Thomas, S. Gehrke and B. Kirchner, *J. Chem. Phys.*, 2020, **152**, 164105.
43 H. J. Gores, J. Barthel, S. Zugmann, D. Moosbauer, M. Amereller, R. Hartl and A. Maurer, in *Handbook of Battery Materials*, ed. C. Daniel and J. O. Besenhard, Wiley, 1st edn, 2011, pp. 525–626.
44 J. Han, A. Mariani, S. Passerini and A. Varzi, *Energy Environ. Sci.*, 2023, **16**, 1480–1501.
45 J. Wang, Y. Yamada, K. Sodeyama, C. H. Chiang, Y. Tateyama and A. Yamada, *Nat. Commun.*, 2016, **7**, 12032.
46 J. Fawdon, J. Ihli, F. L. Mantia and M. Pasta, *Nat. Commun.*, 2021, **12**, 4053.
47 B. Cartigny, N. Azaroual, M. Imbenotte, N. Sadeg, F. Testart, J. Richecoeur, G. Vermeersch and M. Lhermitte, *J. Anal. Toxicol.*, 2001, **25**, 270–274.
48 P. R. Leger, R. A. Murphy, E. Pushkarskaya and R. Sarpong, *Chem. – Eur. J.*, 2015, **21**, 4377–4383.
49 E. Posnjak, *J. Phys. Chem.*, 1928, **32**, 354–359.
50 Z. Chen, L. Wang, J. Zheng, Y. Huang, H. Huang, C. Li, Y. Shao, X. Wu, X. Rui, X. Tao, H. Yang and Y. Yu, *ACS Nano*, 2024, **18**, 8496–8510.
51 J. Park, G. Oh, U. Kim, M. H. Alfaruqi, X. Xu, Y. Liu, S. Xiong, A. T. Zikri, Y. Sun, J. Kim and J. Hwang, *Adv. Sci.*, 2023, **10**, 2301201.
52 W. Wang, Y. Wang, C.-H. Wang, Y.-W. Yang and Y.-C. Lu, *Energy Storage Mater.*, 2021, **36**, 341–346.
53 Z. Yu, Q. Liu, C. Chen, Y. Zhu and B. Zhang, *J. Power Sources*, 2023, **557**, 232592.
54 B. Lamontagne, F. Semond and D. Roy, *Surf. Sci.*, 1995, **327**, 371–378.
55 Y. Pang, Q. Lai, H. Xia, W. Zhang, H. Chen, R. Chen, Z. Lin and J. Zheng, *ACS Appl. Mater. Interfaces*, 2024, **16**, 70606–70617.
56 Z. Jiang, N. Li, L. Li, F. Tan, J. Huang and S. Huang, *Adv. Mater.*, 2024, **36**, 2311127.
57 X. Ren, M. He, N. Xiao, W. D. McCulloch and Y. Wu, *Adv. Energy Mater.*, 2017, **7**, 201601080.
58 X. Guo, R. Markowski, A. Black, P. Apostol, D. Rambabu, O. Lužanin, T. Pavčnik, D. Monti, M. Du, D. Tie, X. Lin, V. R. Bakuru, R. Delogne, K. Robeyns, L. Simonelli, J.-F. Gohy, J. Bitenc, J. Wang, A. Ponrouch and A. Vlad, *Energy Environ. Sci.*, 2025, **18**, 9114–9124.